RSC Advances

ROYAL SOCIETY OF CHEMISTRY

www.rsc.org/advances

Electrochemical route for accessing amorphous mixed-metal hydroxides nanospheres and magnetism

H. B. Li, Y. Q. Gao, G. W. Yang *

State Key Laboratory of Optoelectronic Materials and Technologies, Nanotechnology Research Center, School of Physics & Engineering, Sun Yat-sen University, Guangzhou 510275, Guangdong, P. R. China

Abstract

A series of amorphous mixed-metal hydroxides nanospheres with a homogeneous distribution of metals in compositions including binary Fe-Co, Fe-Ni and Co-Ni hydroxides and ternary Ni-Co-Fe hydroxides have been, for the first time, prepared *via* a simple, facile and green electrochemical technique. The morphology, structure and element distribution of the as-prepared amorphous nanophases were characterized in detail. The magnetic measurements showed that all the as-prepared amorphous nanophases exhibit similar magnetic behaviors for their clear magnetic hysteresis loops and well saturated magnetization, and the amorphous Fe-Co hydroxide nanospheres have the highest saturation magnetization (160.7 emu g^{-1}) at room temperature among four amorphous nanophases. These findings pave a way to applications of amorphous metal hydroxides nanomaterials as magnetic materials.

*Corresponding authors: stsygw@mail.sysu.edu.cn,

1. Introduction

Transitional metal oxides and hydroxides nanomaterials have attracted considerable attention due to their wide applications in many fields [1-4]. The chemical and physical properties of nanomaterials not only depend on their size, morphology and phase structure but also are influenced by their composition. The single-component metal oxides and hydroxides with various nanostructures have been widely studied due to their excellent magnetic, electric, electrochemical and optical properties [5-7]. Recent efforts have been focus on the development of transitional oxides and hydroxides nanomaterials with more complex metal compositions for their novel properties beyond each individual component [8-12]. Among the numerous transition metals, cobalt- and nickel- based hydroxides with more complex metal compositions have been extensively studied for their large scale applications as supercapacitor electrodes [13-16], water oxidation catalysts [17] and so on. However, much few attentions have been focus on investigation of the amorphous transitional mixed-metal hydroxides nanomaterials and their magnetic properties. In fact, the amorphous metal hydroxide nanomaterials are usually great potential as magnetic materials due to the unique magnetic behaviors [18].

For this issue, herein, we report that a series of amorphous binary mixed-metal (Ni-Co, Ni-Fe and Fe-Co) hydroxides and ternary mixed-metal (Ni-Co-Fe) hydroxides nanospheres with a homogeneous distribution of metals are prepared by a simple, facile, environmentally friendly and low-cost electrochemical method in an ambient environment. The magnetic performance of the as-prepared amorphous phase

products with multiple-components are fully characterized. Interestingly, our measurements show that the amorphous Fe-Co hydroxide nanospheres exhibit the highest saturation magnetization among these four amorphous phases. Note that, the values of saturation and residual magnetization increase with the Fe content increasing, while the value of coercivity is negatively correlated with Fe content.

2. Experimental

The amorphous transitional mixed-metal hydroxides are prepared by an idiographic electrochemical method and the setup is shown in Fig. 1. The detailed description of this technique has been reported in our previous works [18-19]. In this case of amorphous mixed-metal hydroxides, the samples are cathodically deposited onto a graphite substrate with a size of 2.0 × 1.0 cm^2 under a constant potential mode. The deposition bath contains two parallel graphite sheets as work electrodes, the high-purity de-ionized water (18.2 MΩ cm) as electrolyte, and an alloy target as metal resource at the center of the bath floor. The experiments are conducted at room temperature. In detail, the Fe-Co-Ni hydroxides can be prepared by this method with the ternary Fe-Co-Ni alloy target (molar ratio of Fe/Co/Ni is 1:1:1) at the center of the bath floor under a constant potential of 90 V. The binary Fe-Co, Fe-Ni and Co-Ni hydroxides can be prepared with the binary alloy target, Fe-Co alloy (molar ratio Fe/Co is 1:1), Fe-Ni alloy (molar ratio Fe/Ni is 1:1) and Co-Ni alloy (molar ratio Co/Ni is 1:1), respectively. The experiments are carried out under a constant potential mode with a constant potential voltage of 90 V.

Scanning electron microscopy (SEM, JSM-7600F), transmission electron microscopy (TEM, FEI Tecnsi G2 F30) and X-ray diffraction (XRD) pattern are employed to identify the structure, morphology and microstructure of the as-prepared samples. The chemical composition and distribution of the products are collected by the energy-filter TEM mapping. X-ray photoelectron spectroscopy (XPS, ESCA Lab250) is employed to probe the surface chemical binding energies of the as-prepared samples. Raman spectra are collected on an argon-ion laser micro-Raman spectrometer (Renishaw inVia) with an incident wavelength of 785 nm. The mass of the as-prepared samples are evaluated by a XP2U Ultra-microbalance (d = 0.1 μg). The gravimetric nickel, cobalt and iron are measured by using the inductively coupled plasma (ICP, iCAP 6500).

Magnetization measurements are carried out on a Magnetic Property Measurement System (MPMS XL-7) from Quantum Design. The hysteresis loops are measured at low temperature (2 and 20 K) and room temperature (300 K) in an external magnetic fields ranging from -15 to 15 KOe. Zero-field-cooled (ZFC) and field-cooled (FC) magnetization curves (M(T) from 2 to 300 K) of amorphous mixed-metal hydroxides under an external magnetic field of 100 Oe are obtained.

3. Results and Discussion

The size and morphology of the products are analyzed by SEM (Fig. 2) and TEM (Fig. 3-4). Typical SEM images of the as-prepared Fe-Co-Ni (Fig. 2a-b), Fe-Co (Fig. 2c-d), Co-Ni (Fig. 2e-f) and Fe-Ni hydroxides (Fig. 2g-h) show that the as-prepared

samples are composed of many well-defined nanospheres with roughness surfaces. The average diameter of these nanospheres is about 200 nm. Typical TEM images, the corresponding selected-area electron-diffraction (SAED) pattern and the corresponding element mapping images of the Co-Ni samples are shown in Fig. $3a_1$-a_5. Clearly, a broad and diffused halo ring is observed in the SAED pattern (Fig. $3a_2$), which indicating a amorphous phase. The element mapping images (Fig. $3a_3$-a_5) suggest that the distribution of elements O, Co and Ni is homogeneous, which indicating a homogeneous distribution of metals in the amorphous. The same analysis is taken for the Fe-Co (Fig. $3b_1$-b_5), Fe-Ni (Fig. $3c_1$-c_5) and Fe-Co-Ni samples (Fig. 4). Therefore, these results show that the as-prepared products are the amorphous phase and have a homogeneous structure. From the ICP analysis, it is found that the molar ratio of Co/Ni, Co/Fe, Ni/Fe and Ni/Co/Fe atoms in the as-prepared samples can be estimated to be 1:1, 3:2, 7:3 and 4:4:3, respectively.

XPS is a reliable method to study the chemical states of bonded elements on the material surface by measuring the binding energy. XPS spectra of the amorphous products are shown in Fig. 5-6. In detail, the O 1s spectra of all the products as shown in Fig. 5 (a_3, b_3, c_3) and Fig. 6d present a main peak centered at a binding energy of 531.1-531.4 eV, which indicates that the oxygen is in the form of bound hydroxide groups (OH^-) suggesting the formation of M-OH (M = Co, Ni, Fe) [20-22]. For all the O 1s spectra, a second higher binding energy peak at 532.5-532.9 eV appears, which can be assigned to contributions of adsorbed water [20]. Fig. 5 (a_1, b_1) and Fig. 6b show the Co $2p_{3/2}$ spectra of different samples with a main binding energy peak

centered at 781.5, 780.9 and 780.8 eV, respectively. These peaks can be attributed to Co^{2+} in mixed-metal hydroxides [16, 20, 24]. Furthermore, the broad peak in Fig. $5b_1$ is fitted by containing a weak peak at 777.6 eV resulting from cobalt element. The main peaks centered at 856.0, 855.8 and 855.7 eV with a shakeup satellite peak at 861.9 eV in the Ni $2p_{3/2}$ spectra as shown in Fig. 5(a_2, c_1) and Fig. 6a are related to Ni^{2+} formation in mixed-metal hydroxides [22-24]. A major binding energy peak at 712.2 eV (Fig. $5c_2$ and Fig. 6c) and 711.3 eV (Fig. $5b_2$) in the Fe $2p_{3/2}$ spectra indicates that iron is in the form of Fe^{3+} in the samples [20, 24]. Thus, XPS studies confirm the formation of mixed-metal hydroxides including binary mixtures Fe-Co, Fe-Ni and Co-Ni and ternary mixture Ni-Co-Fe hydroxides.

The formation of mixed-metal hydroxides is further confirmed by the Raman spectroscopy as shown in Fig. 7. In detail, the spectrum of the Co-Ni hydroxide (Fig. 7a) shows the bands at 189, 253, 304, 470, 533 and 660 cm^{-1}. The bands at 304, 470 and 533 cm^{-1} are indicative of $Ni(OH)_2$ phase [25] and the bands at 189, 253, 470, 533 and 660 cm^{-1} are indicative of $Co(OH)_2$ phase [26]. The band at 533 cm^{-1}, broadened and strongest, can be assigned to vibrations of the Ni−O/Co−O symmetric stretching (Ag) mode [25-28]. The peak located at 470 cm^{-1} corresponds to an Ni−OH/Co−OH symmetric ($A_{1g(T)}$) mode. The peak at 304 cm^{-1} can be due to $E_{g(T)}$ mode for $Ni(OH)_2$. The band at 189 and 253 are indicative E_g symmetry and 660 cm^{-1} is A_{1g} symmetry for a cobalt hydroxide phase. Fig. 7b presents the bands at 191, 478, 518, 612 and 680 cm^{-1}, which represent of a Fe-Co hydroxide. Three peaks of 191, 478 and 680 cm^{-1}, which dominate the spectrum, reflect E_g symmetry, Fe−OH/Co−OH symmetric

($A_{1g(T)}$) mode and Fe-O/Co−O symmetric stretching (Ag) mode, respectively [25-28]. The Raman bands located at 244, 533 and 648 cm^{-1} (Fig. 7c) can correspond to a Fe-Ni hydroxide phase. Ten peaks at 166, 202, 254, 308, 376,431,550, 631, 700 and 785 cm^{-1} shown in Fig. 7d are assigned to a Fe-Co-Ni hydroxide phase. Figure 7e shows the XRD patterns of all the amorphous products with no peaks being present apart from the graphite substrate's peaks.

Based on these results above, we can conclude that the amorphous mixed-metal hydroxides are prepared in our studies. The unique technique has the following advantages. Firstly, this method is simply and easily to operated since amorphous phases can be prepared only in one step. Secondly, this technique is green and no pollution to the environment. The highly pure de-ionized water as the electrolyte provides a chemically clean reaction environment without any chemical additives, which not only ensures clean surface of productions, but also ensure no chemical pollution to the environment. Thirdly, the composition of amorphous phases is controllable for the composition of mixed-metal hydroxides by controlling the alloy target component. Finally, the amorphous products can be deposited on different substrates directly which make the products have a sufficient contact with the substrate.

Temperature dependent magnetization M(T) curves at an applied magnetic field (H) of 100 Oe are measured for all amorphous as-prepared samples under ZFC and FC conditions (from 2 to 300 K) and the field dependent magnetization M(H) curves are measured at three different temperatures 2, 20 and 300 K. ZFC and FC curves of

the amorphous Co-Ni hydroxides are shown in Fig. 8a. Clearly, we can see that, below 300 K, the M_{ZFC} value is always smaller than the M_{FC} value and no bifurcation point appears between the ZFC and FC curves, which indicating the blocking temperature is above the 300 K. The FC magnetization of the sample continuously decreases with the temperature increasing, which can be assigned to the weak interaction or non-interaction between nanospheres [29].

Fig. 8b shows the field-dependent curves of the amorphous Co-Ni hydroxides measured at 2, 20 and 300 K. The field-dependent magnetization curves show a nonlinear evolution of the fraction with a saturation value (M_S) of 16.6 (300 K), 22.7 (20 K) and 27.2 emu g^{-1} (2 K) at 15 kOe. Clearly, all the curves perform small hysteresis loop with narrow square shape indicating ferromagnetic behavior below 300 K. Moreover, the hysteresis loop is presented with a coercive field around 83.9, 149.9 and 191.8 Oe at 300, 20 and 2 K, respectively. The residual magnetization (Mr) at 2, 20 and 20 K is about 8.5, 6.1 and 3.8 emu g^{-1}, respectively. Thus, these values are much lower than that of Co-Ni alloy [30]. The higher value of magnetization and hysteresis loop area at lower temperature evidently suggest that, at lower temperature, ferromagnetic ordering is much prominent than that of at room temperature.

Fig. 8c-d present the M(T) and M(H) curves of the amorphous Fe-Co hydroxides. Clearly, the ZFC magnetization of the sample continuously increases with the temperature increasing. We can see that there also no bifurcation point appears between the ZFC and FC curves below 300 K, which indicating the blocking temperature of the amorphous Fe-Co hydroxides is above the 300 K as well as Co-Ni

hydroxides. The value of saturation magnetization at different temperature is 160.7 (300K), 169.4 (20 K) and 171 emu g^{-1} (2 K), respectively. The value of coercivity (Hc) is 42.3 Oe at 300 K, 51.6 Oe at 20 K and 56.3 Oe at 2 K, respectively. The hysteresis loop at different temperatures has little change, and these hysteresis loops at 2 and 20 K overlap especially. The saturation magnetization of our products obtained has much higher values than that of those of Co–Fe layered double hydroxide obtained [31].

Fig. 8e-f show the M(T) and M(H) curves of the amorphous Fe-Ni hydroxides samples. The ZFC curve presents one narrow peak at 11.9 K, which is usually corresponded to the mean blocking temperature (T_B). It can be seen that amorphous Fe-Ni hydroxides exhibit clear magnetic hysteresis loops, and the values of magnetization at different temperatures are well saturated. The values of Hc and Mr are given in Fig. 8f. These Ms and Mr values are lower than that of the Fe-Ni alloy in previous report [32].

Temperature-dependent curves (from 2-300 K) and field-dependent curves (at 2, 20 and 300K) of the amorphous Fe-Co-Ni hydroxides are show in Fig. 8g-h, respectively. There no bifurcation point appearance between the ZFC and FC curves. The blocking temperature can reach to 55 K. Note that, below 300 K, a series of narrow square shape hysteresis loops are presented in Fig. 8h. The values of Hc and Mr are shown in Fig. 8h. All above results suggest that the amorphous Fe-Co-Ni hydroxides possess ferromagnetic behaviors below room temperature. In addition, since the magnetic hysteresis loops of ferrimagnets have the similar shape with that of ferromagnets, the prepared products in our case are also likely to ferrimagnetic.

Furthermore, the high temperature dependent magnetization M(T) curve at an applied magnetic field (H) of 1000 Oe is measured for the amorphous Co-Ni hydroxides as shown in Figure 9. The magnetization of the sample decreases slowly with the temperature increasing, and no Curie point emerges.

It can be concluded from above the analysis that all the samples exhibit similar magnetic behaviors for their clear magnetic hysteresis loops and well saturated magnetization. The values of M_S and M_r increase with the Fe content increasing, but the value of H_c negatively correlated with Fe content. The high magnetizations (M_S and M_r) can be attributed to the uncompensated surface spins are frozen in the direction of the magnetic field at low temperatures (below T_B) [33].

The values of H_c obtained by our products are small indicating a low magnetic loss. Magnetic thin films have been widely used in many high frequency devices, such as micro-inductors, magnetic sensors and so on [34, 35]. Furthermore, magnetic nanoparticles can be used to enhance the sensitivity and the stability of biosensors and sensors for the detection of some analyses in environmental and food applications [36]. In addition, the hydroxides can be used as precursors to ferrite spinels, most widely used magnetic materials [31]. Additionally, recent research has demonstrated that mixed-metal hydroxide compounds such as Co-Ni hydroxides, have advantages over single composition ones as the positive electrode materials of supercapacitors due to mixed-metal compounds greatly promoting the integrated electrochemical performance [37, 38].

Now we turn to the position to discuss the formation of amorphous phases upon

our electrochemistry. We take the amorphous Co-Ni hydroxide formation as an example to address the basic physics and chemistry involved in the preparations of the amorphous mixed metal hydroxides. A relevant mechanism is as shown in Fig. 1. Simply, two processes can be divided as follows. (i) When the Co-Ni alloy target is immersed in pure de-ionized water (18.2 MΩ cm), it can be polarized and releases a small quantity of metal ion (Ni^{2+} and Co^{2+}) and e^-, adhered on the surface of alloy target. (ii) Under the influence of an extra electric field, Ni^{2+} and Co^{2+} move toward to the cathode. Due to nickel more active than hydrogen, H^+ gets e^- more easily than Ni^{2+} / Co^{2+}. Meanwhile, bubbles are observed on the surface of cathode conformed above conjecture. Finally, Ni^{2+} and Co^{2+} react with OH^- then form into Co-Ni hydroxide deposited on the cathode surface. The electrochemical reactions take place on the cathode as follows

$$Ni^{2+} + Co^{2+} + 4OH^- \rightarrow Ni\text{-}Co(OH)_4 \quad (1)$$

$$2H^+ + 2e^- \rightarrow H_2 \quad (2)$$

At the same time, H^+ moves toward to the surface of the Co-Ni alloy target and OH^- moves toward to the anode under the influence of an extra electric field. In the same way, bubbles are also observed on the surface of anode. The electrochemical reactions take place on the anode as follows

$$4OH^- - 4e^- \rightarrow O_2 + 2H_2O \quad (3)$$

In addition, other transition metal hydroxides or oxides can be fabricated by this method. For example, manganese hydroxide or oxide can be prepared by change the target to manganese target [39, 40].

4. Conclusion

In summary, the amorphous transitional mixed-metal hydroxides nanospheres with a homogeneous distribution of metals have been prepared via a simple, green and low-cost electrochemical route. The as-prepared amorphous phases exhibited similar magnetic behaviors for their clear magnetic hysteresis loops and well saturated magnetization. The amorphous Fe-Co hydroxide nanospheres have the highest saturation magnetization (160.7 emu g^{-1} at room temperature) among these amorphous phases. The values of M_S and M_r increase with the Fe content increasing, but the value of H_c negatively correlated with Fe content in our case. These investigations pave a way to applications of amorphous mixed-metal hydroxide nanomaterials as magnetic materials.

Acknowledgement. NSFC (U0734004) and the State Key Laboratory of Optoelectronic Materials and Technologies of Sun Yat-sen University supported this work.

References

[1] Gao, M.; Sheng, W.; Zhuang, Z.; Fang, Q.; Gu, S.; Jiang, J.; Yan, Y. Efficient Water Oxidation Using Nanostructured α Nickel-Hydroxide as an Electrocatalyst, *J. Am. Chem. Soc*. **2014**, *136*, 7077−7084.

[2] Choi, B. G. *et al.*, Enhanced Pseudocapacitance of Ionic Liquid/Cobalt Hydroxide Nanohybrids, *ACS Nano* **2013**, *3,* 2453-2460.

[3] Liang, Y.; Li, Y.; Wang, H.; Zhou, J.; Wang, J.; Regier, T.; Dai, H. Co_3O_4 Nanocrystals on Graphene as a Synergistic Catalyst for Oxygen Reduction Reaction, *Nature Mater.* **2011**, *10*,780–786.

[4] Du, X.; Wang, C.; Chen, M.; Jiao, Y.; Wang, J. Electrochemical Performances of Nanoparticle Fe_3O_4/Activated Carbon Supercapacitor Using KOH Electrolyte Solution, *J. Phys. Chem. C* **2009**, *113,* 2643–2646.

[5] Chakrabarty, S.; De, K.; Das, S.; Amara, V. S.; Chatterjee, K. General Route to Synthesize of Metal (Ni, Co, Mn, Fe)Oxide Nanostructure and their Optical and Magnetic Behavior, *J. Nanosci. Nanotechnol.* **2013**, *13*, 1–9.

[6] Wang, H. L.; Casalongue, H. S.; Liang, Y. Y.; Dai, H. J. Ni(OH)2 Nanoplates Grown on Graphene as Advanced Electrochemical Pseudocapacitor Materials. *J. Am. Chem. Soc.* **2010**, *132*, 7472–7477.

[7] Yan, J. *et al.* Advanced Asymmetric Supercapacitors Based on $Ni(OH)_2$ /graphene and Porous Graphene Electrodes with high Energy Density. *Adv. Funct. Mater.* **2012**, *22*, 2632–2641.

[8] Louie, M. W.; Bell, A. T. An Investigation of Thin-Film Ni−Fe Oxide Catalysts

for the Electrochemical Evolution of Oxygen, *J. Am. Chem. Soc.* **2013**, *135*, 12329−12337.

[9] Kim, S. J.; Lee, Y.; Lee, D. K.; Leea, J. W.; Kang, J. K. Efficient Co–Fe Layered Double Hydroxide Photocatalysts for Water Oxidation under Visible Light, *J. Mater. Chem. A* **2014**, *2*, 4136–4139

[10] Wang, R.; Yan, X. Superior Asymmetric Supercapacitor based on Ni-Co Oxide Nanosheets and Carbon Nanorods, *Sci. Rep.* **2014**, *4*, 3712.

[11] Wang, H.; Gao, Q.; Hu, J. Asymmetric Capacitor based on Superior Porous Ni–Zn–Co Oxide/hydroxide and Carbon Electrodes, *J. Power Sources* **2010**, *195*, 3017–3024.

[12] Smith, R. D.; Prévot, M. S.; Fagan, R. D.; Trudel, S.; Berlinguette, C. P. Water Oxidation Catalysis: Electrocatalytic Response to Metal Stoichiometry in Amorphous Metal Oxide Films Containing Iron, Cobalt, and Nickel, *J. Am. Chem. Soc.* **2013**, *135*, 11580−11586.

[13] Zhou, D.; Su, X.; Boese, M.; Wang, R.; Zhang, H. $Ni(OH)_2$@$Co(OH)_2$ Hollow Nanohexagons: Controllable Synthesis, Facet-selected Competitive Growth and Capacitance property, *Nano Energy* **2014**, *5*, 52–59.

[14] Chen, G. *et al.* Microwave-assisted Synthesis of Hybrid $Co_xNi_{1-x}(OH)_2$ Nanosheets: Tuning the Composition for high Performance Supercapacitor, *J. Power Sources* **2014**, *251*, 338-343.

[15] Gong, X.; Cheng, J. P.; Liu, F.; Zhang, L.; Zhang, X. Nickel-Cobalt Hydroxide Microspheres Electrodepositioned on Nickel Cobaltite Nanowires Grown on Ni Foam

for High-performance Pseudocapacitors, *J. Power Sources* **2014**, *267*, 610-616.

[16] Patil, U. M. *et al.* Enhanced Supercapacitive Performance of Chemically Grown Cobalt−Nickel Hydroxides on Three-Dimensional Graphene Foam Electrodes, *ACS Appl. Mater. Interfaces* **2014**, *6*, 2450−2458.

[17] Gong, M. *et al.* An Advanced Ni−Fe Layered Double Hydroxide Electrocatalyst for Water Oxidation, *J. Am. Chem. Soc.* **2013**, *135*, 8452−8455.

[18] Li, H. B.; Liu, P.; Liang, Y.; Xiao, J.; Yang, G. W. Amorphous Nickel Hydroxide Nanospheres by Green Electrochemistry Technique: Structure, Morphology and Magnetism, *CrystEngComm* **2013**, *15*, 4054-4057.

[19] Li, H. B. *et al.* Amorphous Nickel Hydroxide Nanospheres with Ultrahigh Capacitance and Energy Density as Electrochemical Pseudocapacitor Materials, *Nat. Commun.* **2013**, *4*, 1894.

[20] Biesinger, M. C.; Payne, B. P.; Grosvenor, A. P.; Lau, L. M.; Gerson, A. R.; Smart, R. St. C Resolving Surface Chemical States in XPS Analysis of first Row Transition Metals, Oxides and Hydroxides: Cr, Mn, Fe, Co and Ni, *Appl. Surf. Sci.* **2011***, 257*, 2717–2730.

[21] Dupin, J. D.; Gonbeau, D.; Vinatierb, P.; Levasseur, A. Systematic XPS Studies of Metal Oxides, Hydroxides and Peroxides, *Phys. Chem. Chem. Phys.* **2000**, *2*, 1319–1324.

[22] Payne, B. P.; Biesinger, M. C.; McIntyrea, N. S. Use of Oxygen/nickel Ratios in the XPS Characterisation of Oxide Phases on Nickel Metal and Nickel Alloy Surfaces, *J. Electron Spectrosc. Relat. Phenomena* **2012**, *185*, 159–166.

[23] Yan, J. *et al.* Advanced Asymmetric Supercapacitors Based on $Ni(OH)_2$ /Graphene and Porous Graphene Electrodes with High nergy Density, *Adv. Funct. Mater.* **2012**, *22*, 2632–2641.

[24] Nai, J.; Tian, Y.; Guan, X.; Guo, L. Pearson's Principle Inspired Generalized Strategy for the Fabrication of Metal Hydroxide and Oxide Nanocages, *J. Am. Chem. Soc.* **2013**, *135*, 16082−16091.

[25] Hermet, P. *et al.* Dielectric, Magnetic, and Phonon Properties of Nickel Hydroxide. *Phys. Rev. B* **2011**, *84*, 235211.

[26] Yang, J.; Liu, H.; Martens, W. N.; Frost, R. L. Synthesis and Characterization of Cobalt Hydroxide, Cobalt Oxyhydroxide, and Cobalt Oxide Nanodiscs, *J. Phys. Chem. C* **2010**, *114*, 111–119.

[27] Chen, R.; Wang, W.; Zhao, X.; Zhang, Y.; Wu, S.; Li, F. Rapid Hydrothermal Synthesis of Magnetic $Co_xNi_{1-x}Fe_2O_4$ Nanoparticles and their Application on Removal of Congo red, *Chem. Eng. J.* **2014**, *242*, 226–233.

[28] Ma, L.; Zhou, K.; Li, Z.; Wei, Q.; Zhang, L. Hot Corrosion of a novel $NiO/NiFe_2O_4$ Composite Coating Thermally Converted from the Electroplated Ni–Fe alloy, *Corrosion Science* **2014**, *53*, 3712–3724.

[29] Winkler, N. *et al.* Surface Spin-glass Freezing in Interacting Core–shell NiO Nanoparticles, *Nanotechnology* **2008**, *19*, 185702

[30] Panday, S.; Daniel, B. S.; Jeevanandam, P. Synthesis of Nanocrystalline Co–Ni Alloys by Precursor Approach and Studies on their Magnetic Properties, *J. Magnetism and Magnetic Materia*ls **2011**, *323*, 2271–2280.

[31] Zhang, X. *et al.* Effect of high Magnetic Field Annealing on the Microstructure and Magnetic Properties of Co–Fe Layered Double Hydroxide, *J. Magnetism and Magnetic Materials* **2010**, *322*, 3023–3027.

[32] Cui, B. Z.; Marinescu, M.; Liu, J. F. High Magnetization Fe-Co and Fe-Ni Submicron and Nanosize Particles by Thermal Decomposition and Hydrogen Reduction, *J. Appl. Phys.* **2014**, *115*, 17A315.

[33] Makhlouf, S. A.; Parker, F. T.; Spada, F. E.; Berkowitz, A. E. Magnetic Anomalies in NiO Nanoparticles, *J. Appl. Phys.* **1997**, *81*, 5561-5563.

[34] Li, D.; Wang, Z.; Han, X. M.; Yue Li, Y.; Guo, X. B.; Zuo, Y. L.; Xi, L. Improved high-frequency soft magnetic films on organic ferroelectric PVDF substrate, *Journal of Magnetism and Magnetic Materials* **2015**, 375, 33–37.

[35] Seemann, K.; Leiste, H.; Ziebert C. Soft magnetic FeCoTaN film cores for new high-frequency CMOS compatible micro-inductors, *Journal of Magnetism and Magnetic Materials* **2007**, 316, 879–882.

[36] Rocha-Santos, T. A.P. Sensors and biosensors based on magnetic nanoparticles, *Trends in Analytical Chemistry* **2014**, 62, 28-36.

[37] Patil, U. M. *et al.* Enhanced Supercapacitive Performance of Chemically Grown Cobalt−Nickel Hydroxides on Three-Dimensional Graphene Foam Electrodes, *ACS Appl. Mater. Interfaces* **2014**, 6, 2450−2458.

[38] Li, H. B.; Gao, Y. Q.; Wang, C. X.; Yang, G. W. Simple electrochemical route for accessing amorphous mixed metal hydroxides for electrode materials of supercapacitors. *Advanced Energy Materials* 2015, **5**, 1401767.

[39] Xia, H.; Zhang, J. W.; Li, X. G. Synthesis of Birnessite-Type MnO_2 by the *In-Situ* Electrochemical Oxidation of Mn_3O_4 Film for Supercapacitors, *Nanoscience and Nanotechnology Letters* **2012**, 4, 559-563.

[40] Xia, H.; Lai, M. O.; Lu L. Nanostructured Manganese Oxide Thin Films as Electrode Material for Supercapacitors, *JOM* **2011**, 63, 54-59

Figure Captions

Figure 1. A schematic illustration of the electrochemistry setup.

Figure 2. SEM images of the amorphous mixed-metal hydroxides deposited on a graphite sheet. (a-b) Fe-Co-Ni hydroxide, (c-d) Co-Ni hydroxide, (e-f) Fe-Co hydroxide and (g- h) Fe-Ni hydroxide.

Figure 3. TEM images of the amorphous mixed-metal hydroxides, the corresponding SAED pattern and the corresponding element mappings. (a_1-a_5) Co-Ni hydroxide, (b_1-b_5) Fe-Co hydroxide and (c_1-c_5) Fe-Ni hydroxide.

Figure 4. (a) TEM image of the amorphous Ni-Co-Fe hydroxides with the inset of the corresponding SAED pattern. (b, c, d and e) element mappings of O, Co, Ni and Fe, respectively.

Figure 5. XPS spectra of (a_1-a_3) Co-Ni hydroxide, (b_1-b_3) Fe-Co hydroxide and (c_1-c_3) Fe-Ni hydroxide.

Figure 6. XPS spectra of Fe-Co-Ni hydroxide: (a) Ni 2p, (b) Co 2p, (c) Fe 2p and (d) O 1s.

Figure 7. Raman patterns of (a) Co-Ni hydroxide, (b) Fe-Co hydroxide, (c) Fe-Ni hydroxide and (d) Fe-Co-Ni hydroxide. (e) XRD patterns of the amorphous products deposited on the graphite.

Figure 8. Magnetization measurement, temperature dependent magnetization M(T) curves and the corresponding hysteresis loops at different temperatures. (a- b) Co-Ni hydroxide, (c- d) Fe-Co hydroxide, (e-f) Fe-Ni hydroxide and (g-h) Fe-Co-Ni hydroxide.

Figure 9. High temperature dependent magnetization M(T) curve of the amorphous Co-Ni hydroxide.

Figure 1

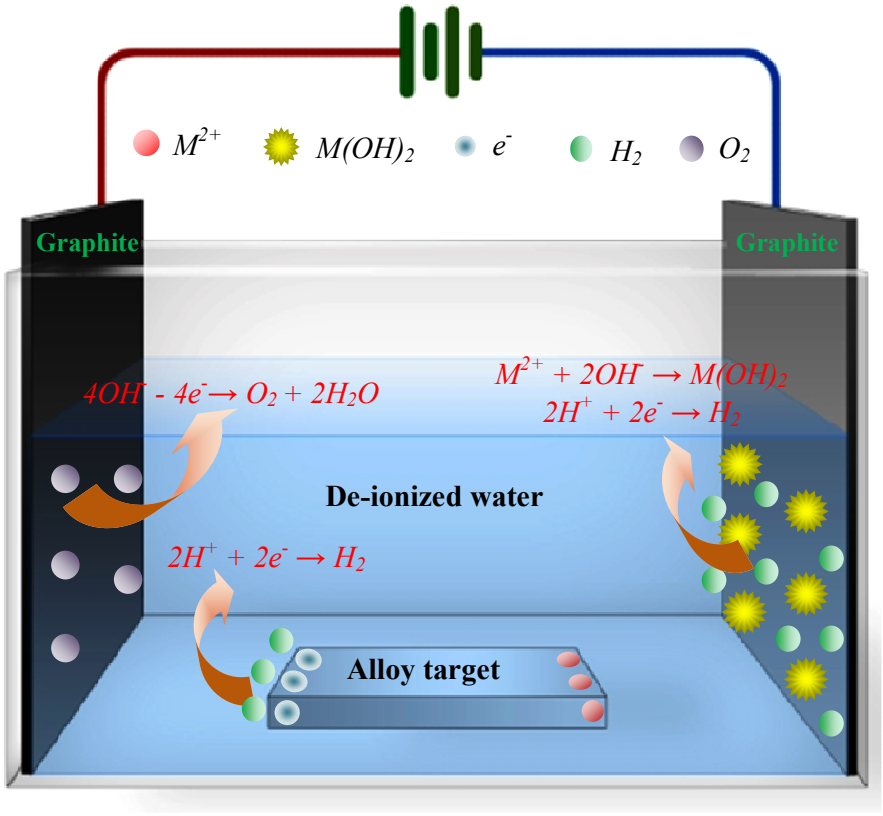

Figure 2

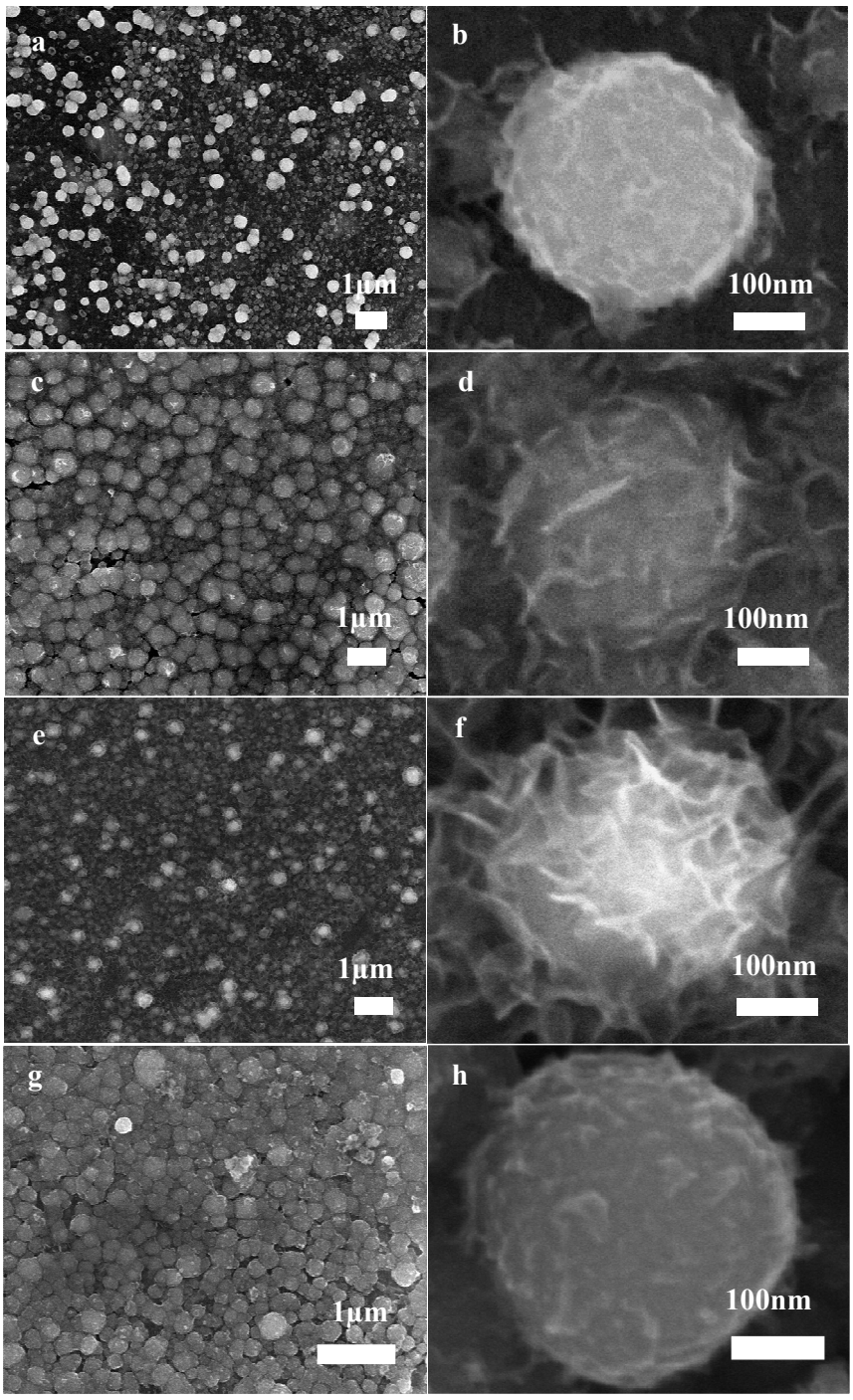

Figure 3

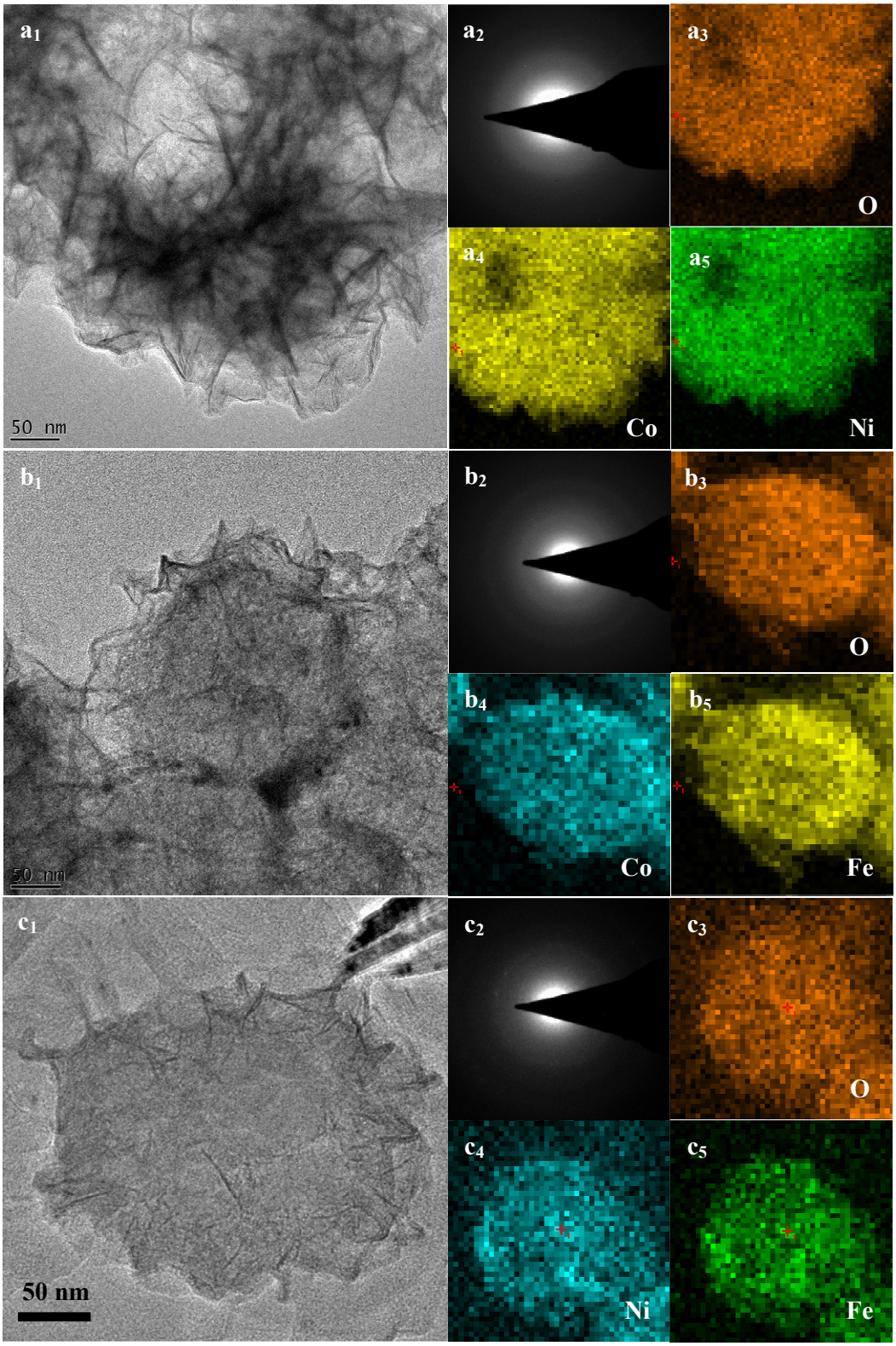

Figure 4

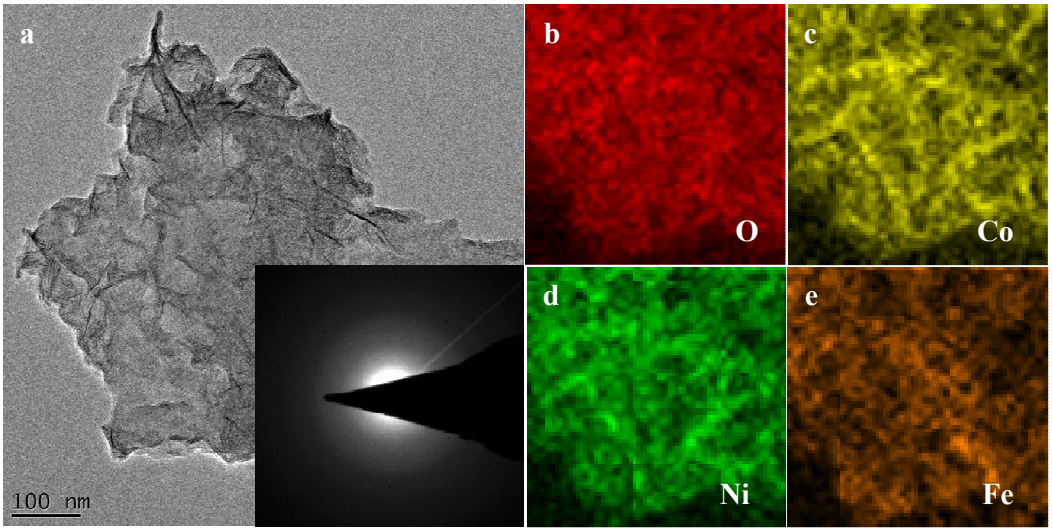

Figure 5

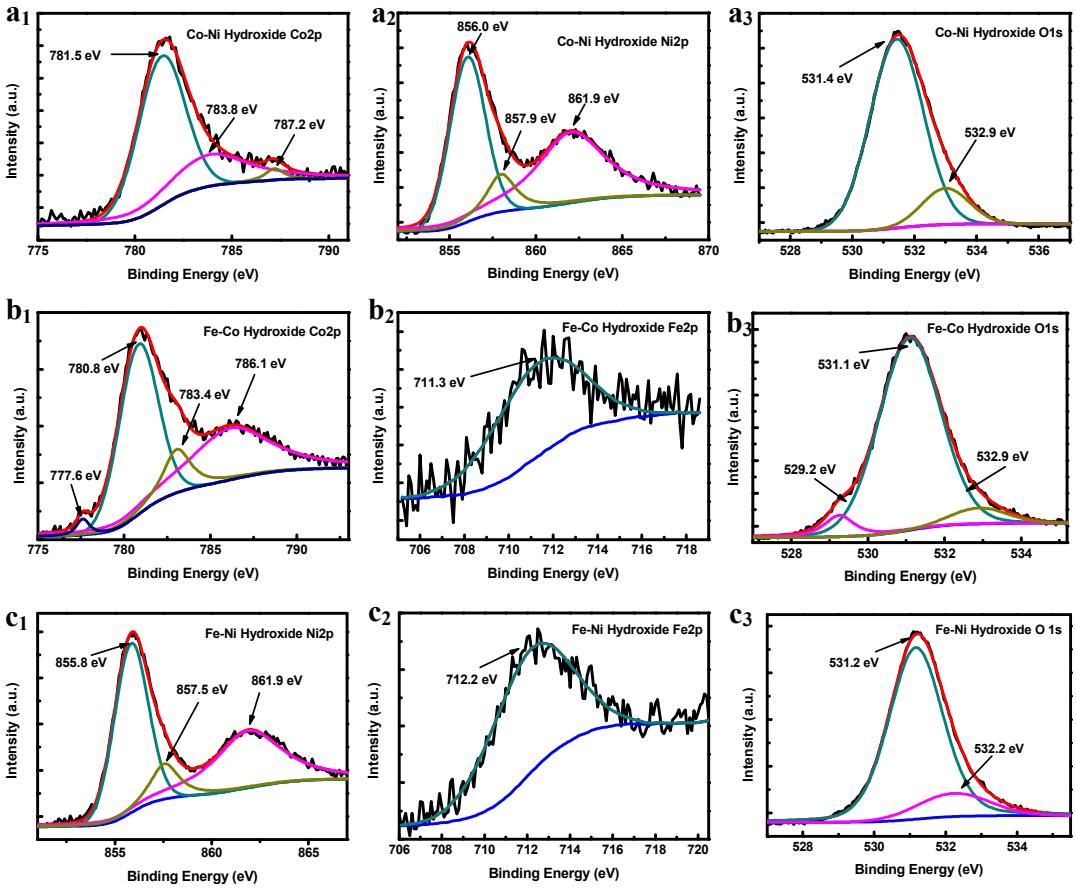

Figure 6

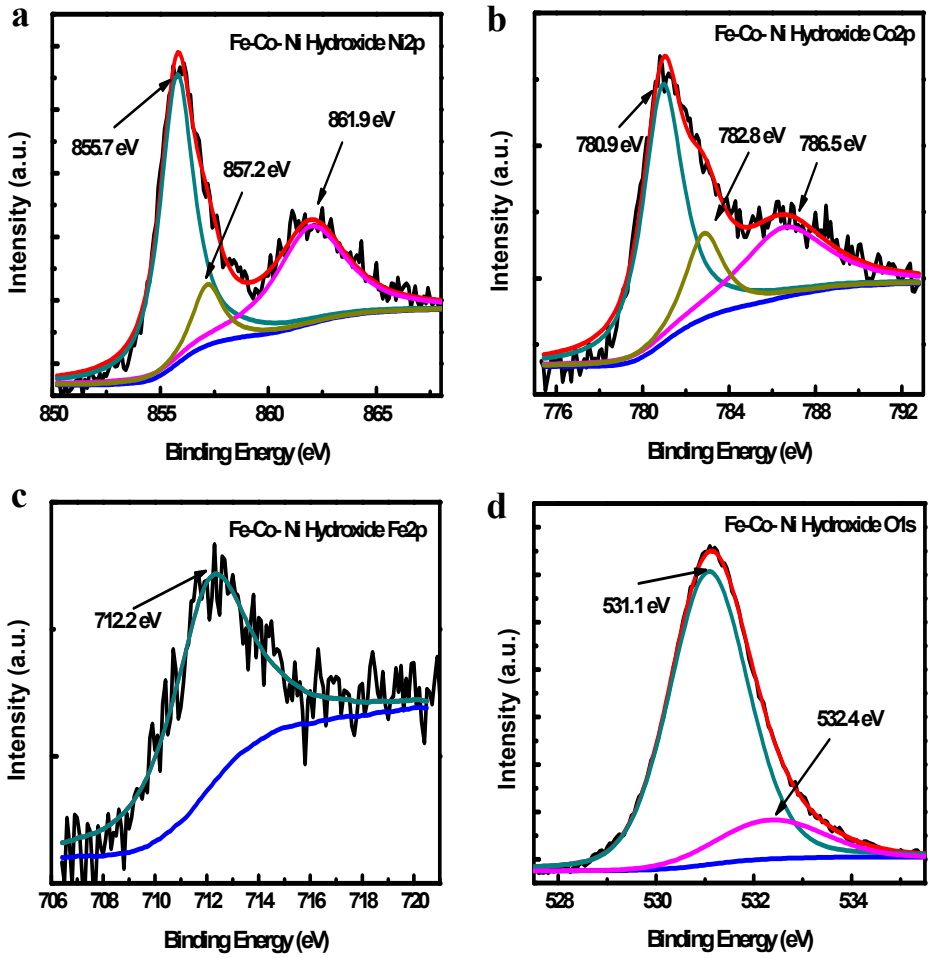

Figure 7

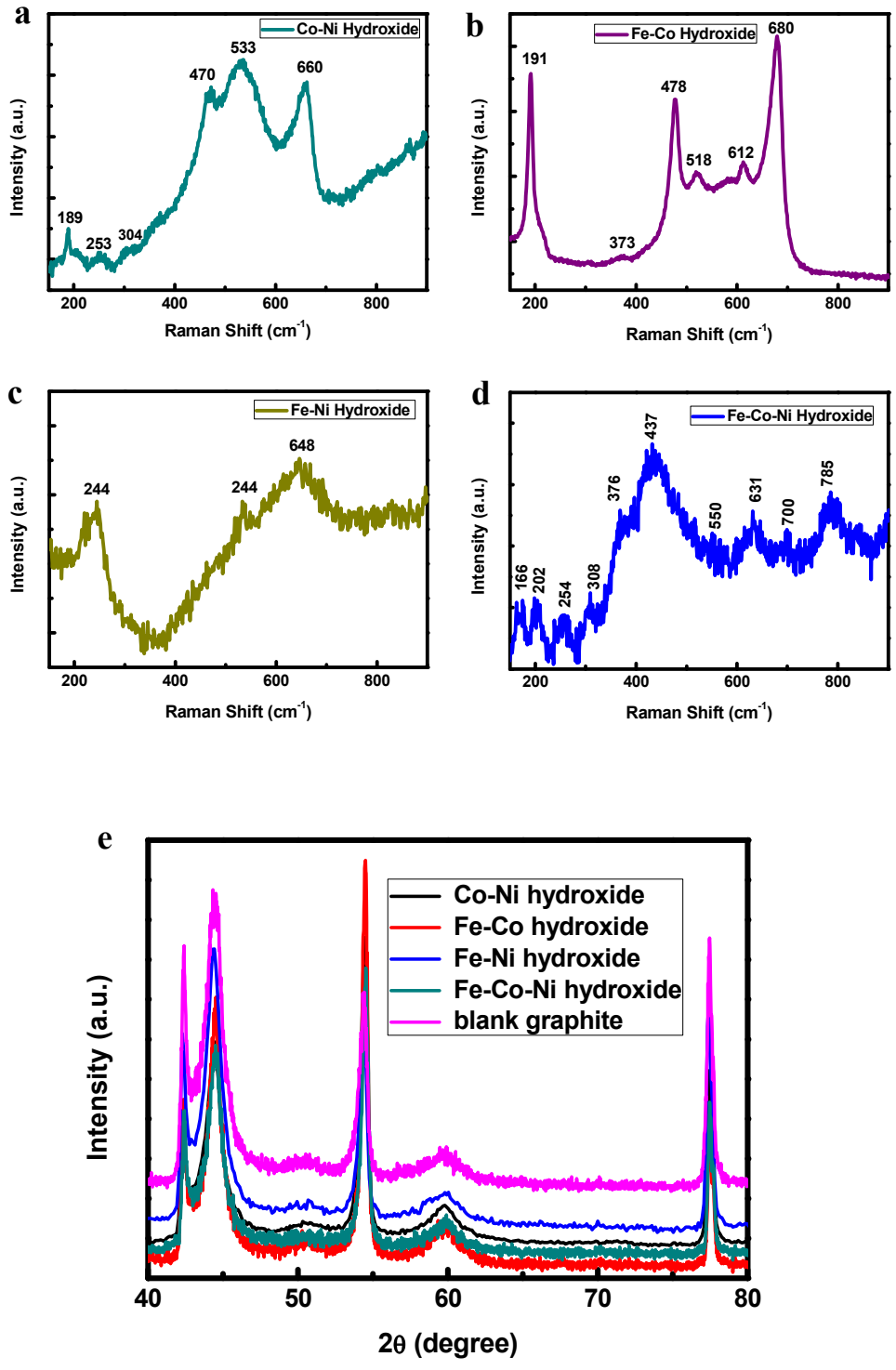

Figure 8

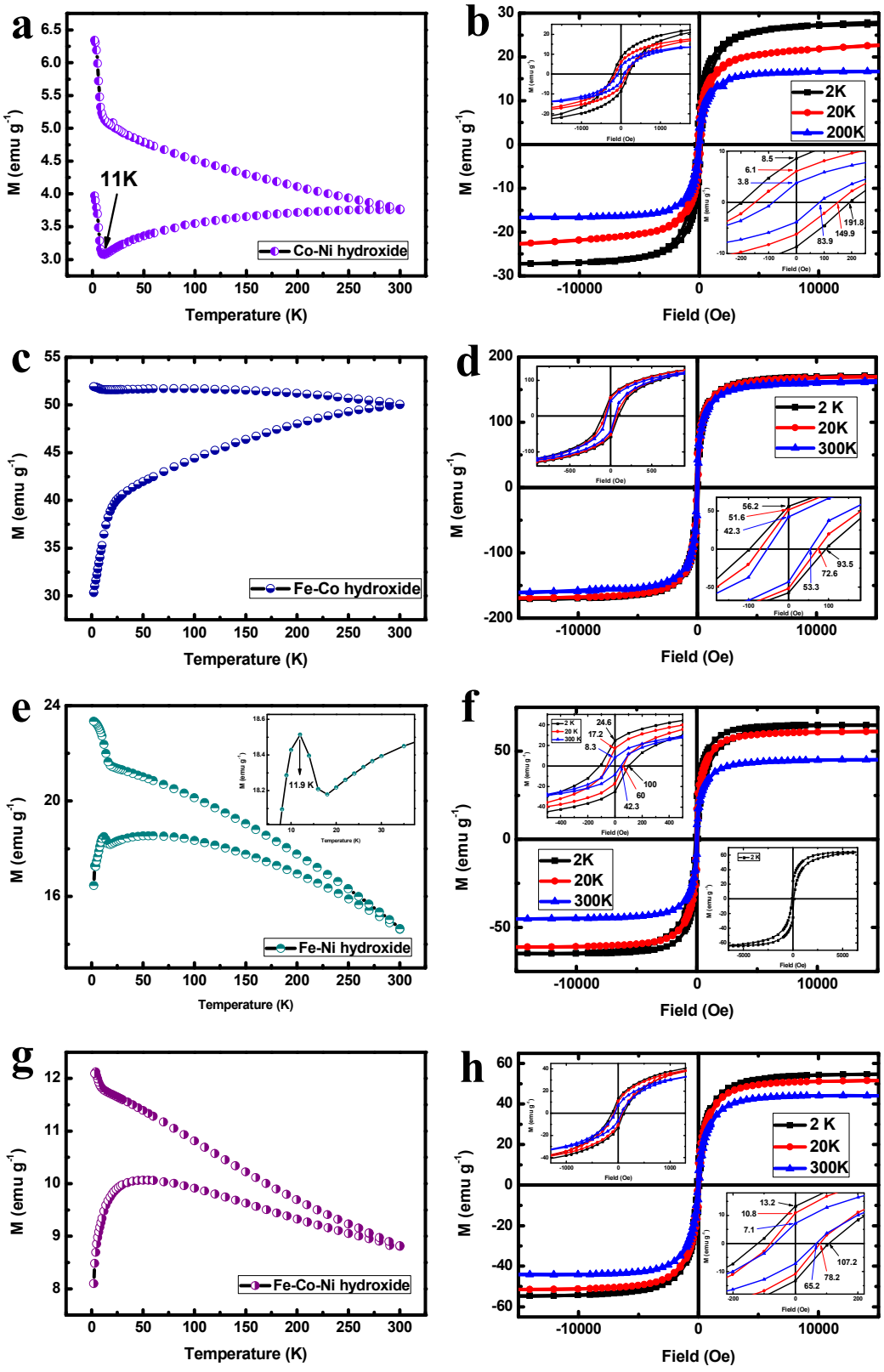

Figure 9